A Compact and Broadband Splitter to Interface Between Strip and Slot Waveguides

Devika Padmakumar Nair and Michaël Ménard, *Member, IEEE*

***Abstract*—We demonstrate a compact and low-loss 1 × 2 power splitter that efficiently splits and couples light from one strip to two slot waveguides. The splitter is optimized over a broad wavelength span ranging from 1.3 to 1.7 μm through finite difference time domain simulations. The splitter junction footprint is only 2.00 × 1.61 μm. The structure does not require an adiabatic transition region and is compatible with standard commercial silicon photonic fabrication processes. Experimental results show an insertion loss of less than 0.7dB for the TE polarization.**

***Index Terms*—Silicon photonics, splitter, multimode interferometer, strip waveguide, slot waveguide.**

I. Introduction

COMPACT and low-loss power splitters are key components in integrated photonic circuits since they are frequently used in modulators [1], multiplexers [2], and optical switches [3]. A number of compact power splitters were demonstrated based on novel optical waveguides, such as Bragg waveguides [4], [5], periodic dielectric waveguides [6], photonic crystal waveguides [7], [8], [9], [10], and plasmonic subwavelength waveguides [11], [12]. Slot waveguides have a unique geometry in which the light propagates within a low refractive index region (slot region) between two high index rails [13], [14]. Unlike other waveguides, slot waveguides enable strong interactions between light and the low index material in the slot. This unique feature prompted the design of various components, such as resonators [15], [16] and polarization beam splitters [17], [18], [19], [20], [21], [22] based on slot waveguides, which led to the implementation of novel sensors [15], [23], [24], modulators [25], [26], and nonlinear optical devices [27].

However, slot waveguides have relatively high propagation losses in comparison to strip waveguides [28]. To minimize losses, slot waveguides are only used in short sections where interactions with the low index material are needed, and strip waveguides are used for guiding light from the source and to the detector. To mitigate the mode mismatch between strip and slot waveguides, different approaches were used to design strip-to-slot waveguide mode converters [28], [29], [30], [31], [32], [33]. Most of these designs can provide a high coupling efficiency but they have sharp corners and small features that are challenging to fabricate. As a result, fabricated devices often provide lower performance than predicted by simulations. Y. Xu et al. proposed a low-loss, MMI based strip-to-slot splitter [34] with a junction footprint of 12.6 × 4.92 μm. This device utilizes an inverse-tapered subwavelength grating (SWG) structure embedded in the center of a multimode waveguide along with two strip-to-slot mode converters integrated at the output ends. Simulation results show promising properties, such as a 200 nm wide operating band, but the device has not been manufactured or tested. Furthermore, its implementation would require a minimum feature size of 59 nm, which is significantly lower than the one typically available from commercial foundries.

Furthermore, most state-of-the-art converters perform only mode conversion between one strip and one slot waveguide, whereas many applications also require 1 × 2 splitting of the power from strip to slot waveguides, such as Mach-Zehnder interferometer (MZI) sensors [23], [24] or modulators [26]. Usually in these devices, a strip-to-slot mode converter is used in the two output arms of a conventional splitter, which increase the size and losses of the device. Additionally, the operating bandwidth can be limited due to its dependence on both the conventional splitter and the strip-to-slot mode converters. To solve these issues, we experimentally demonstrate for the first time to our knowledge a 1 × 2 power splitter junctions that split and convert light from a single strip waveguide to two slot waveguides. The design, fabrication, and characterization of the splitter structures, which are based on a carefully designed multimode junction region that controls the evolution of the optical field and the number of excited modes to minimize losses and maximize the operational wavelength range, is reported. The junctions are optimized for 100, 150, and 180 nm slot output waveguides but the same methodology can be used to design splitters for other slot waveguide geometries. The design is compact, and it overcomes the fabrication limitations imposed by the minimum feature size of commercial photolithographic processes. Simulations are performed over a wide wavelength range of 1300 nm to 1700 nm. The device was successfully fabricated using 193 nm lithography.

II. Design and Optimization

A. Slot Waveguide

Fig. 1(a) shows a schematic of a slot waveguide in which a low refractive index silicon dioxide (SiO_2) slot region is

Received 4 October 2024; revised 2 December 2024; accepted 3 December 2024. Date of publication 16 December 2024; date of current version 31 December 2024. This work was supported in part by the Natural Sciences and Engineering Research Council of Canada, in part by the Fonds de Recherche du Québec-Nature et Technologies, and in part by the Centre d'optique, photonique et laser (COPL). *(Corresponding author: Michaël Ménard.)*

The authors are with the Department of Electrical Engineering, École de Technologie Supérieure (ETS), Montreal, QC H3C 1K3, Canada (e-mail: michael.menard@etsmtl.ca).

Digital Object Identifier 10.1109/JPHOT.2024.3518299

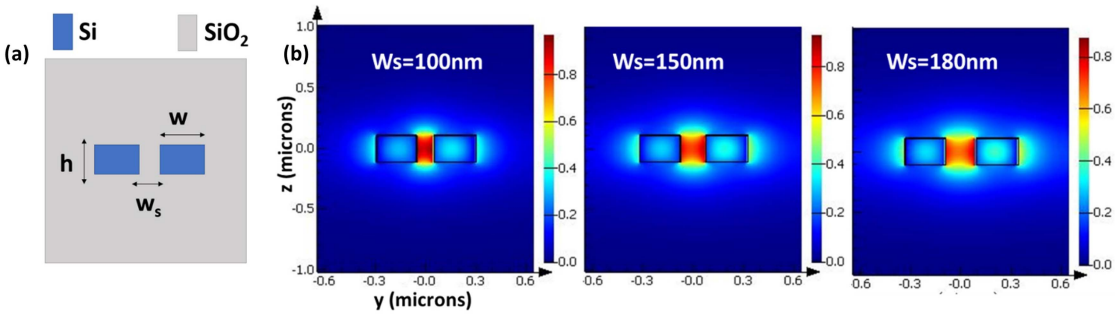

Fig. 1. (a) Geometry of the slot waveguide (h = 220 nm, slot width, w_s = 100 or 150 or 180 nm, w = 250 nm) and (b) simulated normalized field profile of the quasi-TE mode for different slot widths at a wavelength of 1550 nm.

sandwiched between two higher index silicon (Si) rails. The refractive index of the SiO_2 cladding/slot is $n_0 = 1.47$ and the refractive index of the Si rail is $n_1 = 3.50$ at a wavelength of 1550 nm. The height of the Si rails is 220 nm and is constant throughout the device. The width of the silicon rails is 250 nm and three slot widths are considered: 100, 150 and 180 nm. Fig. 1(b) shows the normalized electric field profile for different slot widths.

B. Splitter Design

The splitter junction was designed through a combination of analytical calculations and numerical simulations. A conventional MMI splitter was used as the starting point since the optimization converged to a design achieving significantly better performance than when a Y-branch was used. The initial structure was configured with two output ports, each consisting of one slot waveguide with two rails. The length of the MMI was calculated using the equation $L_{\mathrm{MMI}} = (3L_\pi)$ /4N [35], where N is the number of outputs at the end of the MMI or N-fold images, $L_\pi = \Pi/(\beta_0 - \beta_1)$ which is the beat length, and β_0 and β_1 are the propagation constants of the two lowest order modes, which can be calculated with a finite difference Eigenmode solver [36]. For a MMI with 2 output ports, the length should be between 1.6 to 2.2 μm. The width of the multimode region only supports the TE_0, TE_1,TE_2, TM_0, and TM_1 modes. In order to satisfy this condition, the width must be between 1.45 and 1.80 μm [37]. The next step was to optimize the distance between the two slot waveguides at the output end of the MMI junction. To ensure a balanced output power in the two branches, the junction shape is symmetric along the propagation direction. Finite-difference time-domain (FDTD) simulations were performed to investigate the impact of varying the distance between the two slot waveguide outputs. The simulations showed that in order to achieve an equal splitting of the input signal, a separation of 185 to 255nm between the two output arms of the splitter is required. It is important to note that while the self-imaging principle can provide approximate dimensions, it does not account for all the interactions taking place in the MMI junction, especially when switching from strip to slot waveguides. This adaptation of the self-imaging principle along with the use of FDTD simulations resulted in a flexible design approach that can accommodate variations in waveguide dimensions, particularly when transitioning from strip to slot waveguides with a power splitter.

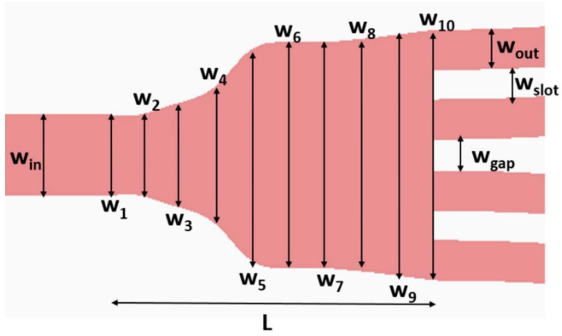

Fig. 2. Splitter layout showing the parameters defined for the optimization.

After calculating these preliminary parameters, a commercial Maxwell solver with a particle swarm optimization algorithm from Ansys Lumerical [37], [38] was used for the final optimization of the device. The primary aim of our power splitter design is to efficiently divide the incoming optical signal with minimal losses over a broad wavelength range, specifically from 1300 nm to 1700 nm. To fulfill this objective, we defined a figure of merit based on the average insertion loss using the formula: $IL = -10log_{10}(mean(T_{\mathrm{net}}))$ where: IL represents the insertion loss, and T_{net} stands for the net transmission into the TE fundamental mode. T_{net} is captured during simulations across 21 frequency points within the specified bandwidth. We then calculate the mean transmission to estimate the average IL over this range. Since the device is constrained to remain symmetrical, the fraction of the input power coupled to only one output port was calculated. Furthermore, the splitter junction was defined by a spline interpolation of 10 polynomials, $w_1 - w_{10}$. Using more polynomials only increased the computation time and did not improve the final results. The geometry of the splitter is presented in Fig. 2. In the polynomials, $w_{\mathrm{in}} = w_1$ was set to 500 nm, which is the width of the input waveguide. The width was gradually increased from w_1 to w_{10} to achieve low coupling losses. A maximum of 50 iterations with a 2.5D FDTD algorithm was used to generate preliminary dimensions and then 3D FDTD was used to refine the design. The parameters of the optimized

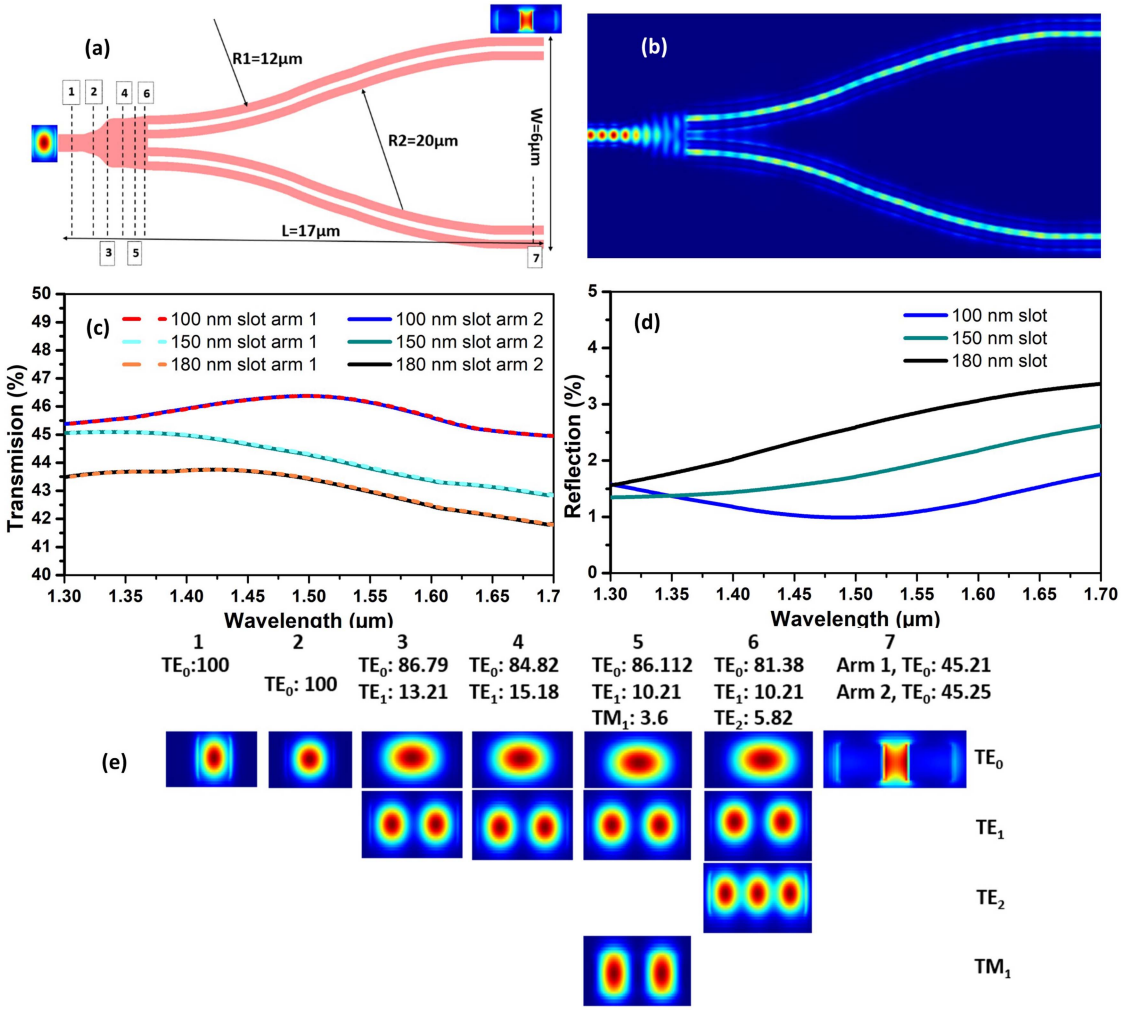

Fig. 3. (a) Geometry of the splitter with optimized slot waveguide output arms, (b) field profile along the splitter at a wavelength of 1550 nm, (c) simulated transmitted power as a function of wavelength in each arm of the splitter, (d) simulated back reflection as a function of wavelength in the optimized splitter, and (e) for cross sections 1– 7, the mode profile and percentage of total power in each mode at a wavelength of 1550 nm for the TE polarization.

TABLE I
MMI JUNCTION WIDTH (μm)

W_{slot}	w_1	w_2	w_3	w_4	w_5	w_6	w_7	w_8	w_9	w_{10}	w_{gap}
0.10	0.5	0.557	0.704	0.94	1.334	1.29	1.35	1.39	1.41	1.4	0.195
0.15	0.5	0.56	0.705	0.95	1.33	1.4	1.47	1.515	1.52	1.52	0.22
0.18	0.5	0.57	0.707	0.96	1.340	1.490	1.56	1.607	1.61	1.61	0.25

junction are shown in Table I. The total length (L) of the junction is only 2 μm, which is very compact. The optimal junction width changes slightly as a function of the slot width ($w_{\mathbf{slot}}$), as shown in Table I.

The output arms of the splitter were further optimized to minimize reflections and scattering losses. Their performance was improved by analyzing the field distribution inside the slot waveguide using FDTD simulations. The output arms of the splitter were configured into two consecutive S-bends with radii of 12 μm and 20 μm, as illustrated in Fig. 3(a). This avoids sharp corners and maximizes transmission at the output of the slot waveguides. The final splitter design, including the input waveguide, splitter junction region and the two bend waveguides at the output end of the splitter, occupies a small area of 17 μm $\times$ 6 μm, which is comparable to or significantly less than that of other state-of-the-art devices [17], [18], [19], [21].

The field intensity profile inside the splitter with 150 nm slot waveguides is shown in Fig. 3(b). There is a weak reflection, which results in ripples at the input side of the splitter. The back reflection was calculated at cross-section 1in Fig. 3(a). Less than 1.5% of the incident light is reflected (see Fig. 3(d)) for the 100 nm slot, less than 2.5% for the 150 nm slot, and less than 3.2% for the 180 nm slot, according to simulations. As per the electric field distribution along the splitter, scattering is negligible. Also, there is no significant excitation of radiation modes in the splitter because the mode is well confined in the silicon waveguide at the input end of splitter and in the slot region at the output of the splitter. For a better understanding of what is happening inside the MMI splitter junction, cross sectional profiles of the excited modes along the device are presented in Fig. 3(e). The power transmitted in each mode along the propagation direction at 1550 nm was calculated using a finite

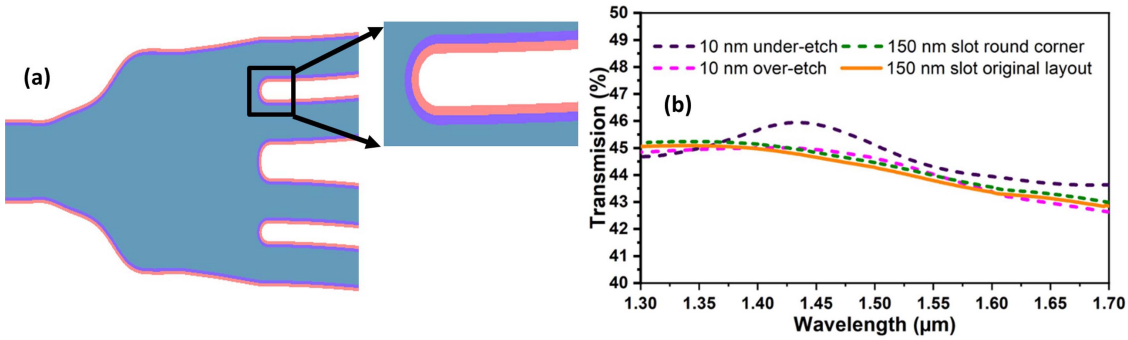

Fig. 4. (a). Optimized splitter geometry with rounded edge and ± 10 nm width variations, (b) Transmission spectra of 150 nm slot splitter showing the impact of fabrication variations.

difference Eigenmode solving algorithm [35]. The percentages of the total power coupled to each mode at 1550 nm were computed at various cross sections as indicated by numbers 1 to 7in Fig. 3(a) and the results are given above the mode profiles in Fig. 3(e). Inside the MMI junction, the highest order modes excited are the TE_2 and TM_1 modes. Avoiding the excitation of higher order modes reduces losses and improves the performance of the splitter.

After the optimization of the junction and output arms, the normalized transmission and reflection spectra (see Fig. 3(b) and (c)) of the structure were calculated using the FDTD software for wavelengths within the range of 1.3 to 1.7 μm with a quasi-TE polarization. Only the TE polarization was considered during the design and testing of the splitter since the TM polarization is not confined within the low index region in the slot waveguides. Thus, there are not benefits to using the TM polarization with these slot waveguides. The normalized transmission power as a function of wavelength is plotted in Fig. 3(c). The average transmitted power at the output of the top/bottom splitter arm is 45.45/46.47% for the 100 nm slot, 43.5/45.2% for the 150 nm slot and 42/44% for the 180 nm slot. The transmission of the device was calculated at cross-section 7in Fig. 3(a), which includes a 13 μm long slot waveguide. Hence, the propagation loss of the slot waveguide bents is included in the overall loss of the splitter. Furthermore, there is very little fluctuations as a function of wavelength in both transmission and reflection over the broad range considered in the simulations. The transmission varies by less than 4% whereas the variation in reflections is less than 3%. The data overlaps because there are no significant variations between the transmission coefficients calculated for each output arm.

The 150 nm slot splitter design was investigated further to assess the impact of manufacturing variations. The effects of rounded corners, and over and under etching by 10 nm (see Fig. 4(a)) were simulated. Fig. 4(b) shows the transmission spectra of the original geometry and of the devices affected by variations in dimensions. Rounding the corners of the output of the junction leads to fluctuations of about 0.1% with respect to the nominal design whereas, for the under-etch dimensions, there is an average of 1% improvement in transmission. This is consistent with our previous observation that the splitter is slightly more efficient for slot waveguides with smaller gaps. In the case of the over etched geometry, there is a ± 0.3% variation across the simulated bandwidth. Therefore, the performance of the splitter remains robust even when there are small variations in dimensions.

III. Fabrication and Characterization

The smallest feature of the splitter is the slot width. For the experimental demonstration, a slot width of 150 nm was used since it is compatible with the design rules of commercial silicon photonic fabrication processes and the simulated transmission loss is less than for a 180 nm slot width. The devices were fabricated using the Advanced Micro Foundry silicon photonics fabrication process. The silicon layer was patterned with 193 nm photolithography before etching the devices. Then, a layer of 2.3 μm of silicon dioxide was deposited to form the top cladding. Light coupling to the chip was achieved with grating couplers (GC) optimized for the TE polarization.

Multiple sets of structures were fabricated to experimentally characterize the splitter. To determine the insertion loss (IL) of the splitter, cascades of Mach-Zehnder interferometers (MZI) (Number of splitters, N = 0, 8, 16, and 24) were used. A single splitter was implemented to determine the splitting ratio and a stand-alone MZI was built to measure its extinction ratio (ER). The case where N = 0 corresponds to two GCs connected by the same number of bent waveguides as the test structures and this was used in order to determine the GC coupling loss and the losses due to propagation. A Scanning Electron Microscope (SEM) image of a fabricated structure is shown in Fig. 5(c).

To test the devices, light from a tunable laser was coupled into them via an 8-degree polished polarization maintaining fiber array and grating couplers. The output was collected in the same way and sent to a photodetector. The transmission spectra of the test structures for the TE polarization over the wavelength range from 1500 nm to 1560 nm, which is the span covered by the grating couplers, are shown in Fig. 5(a). The reference structure (N = 0) loss at a wavelength of 1530 nm is about −11 dB for the TE polarization, which represent the GC insertion loss and the propagation loss in the reference waveguides. The splitter transmission spectra for both arms are shown in Fig. 5(a) and the measured splitting ratio is plotted in Fig. 5(b). A power

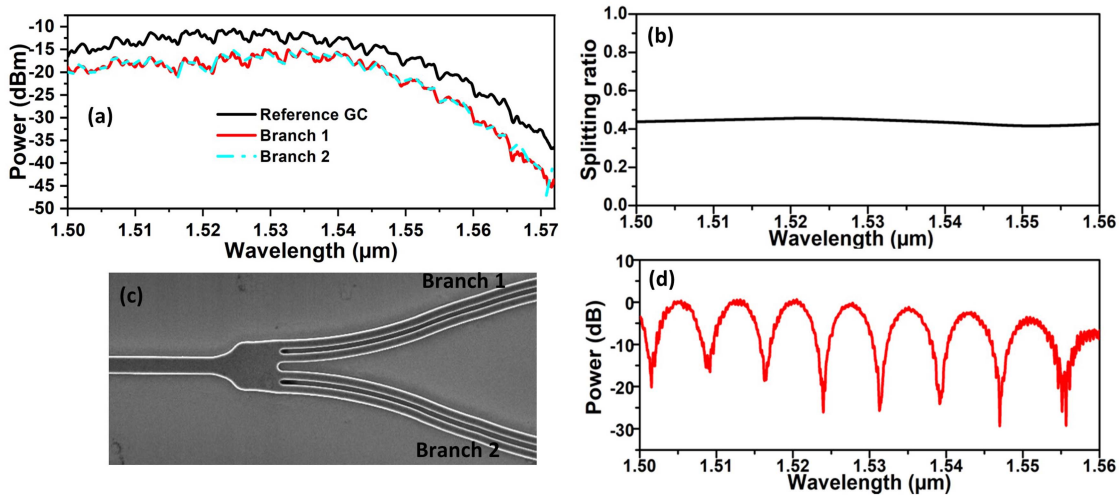

Fig. 5. (a) Measured transmission spectra for both arms of the splitter (branch 2 overlaps branch 1) for the TE polarization including the grating coupler loss, (b) splitting ratio as a function of wavelength, (c) SEM image of a fabricated splitter and (d) transmission spectrum of the MZI with Δ L = 120 m.

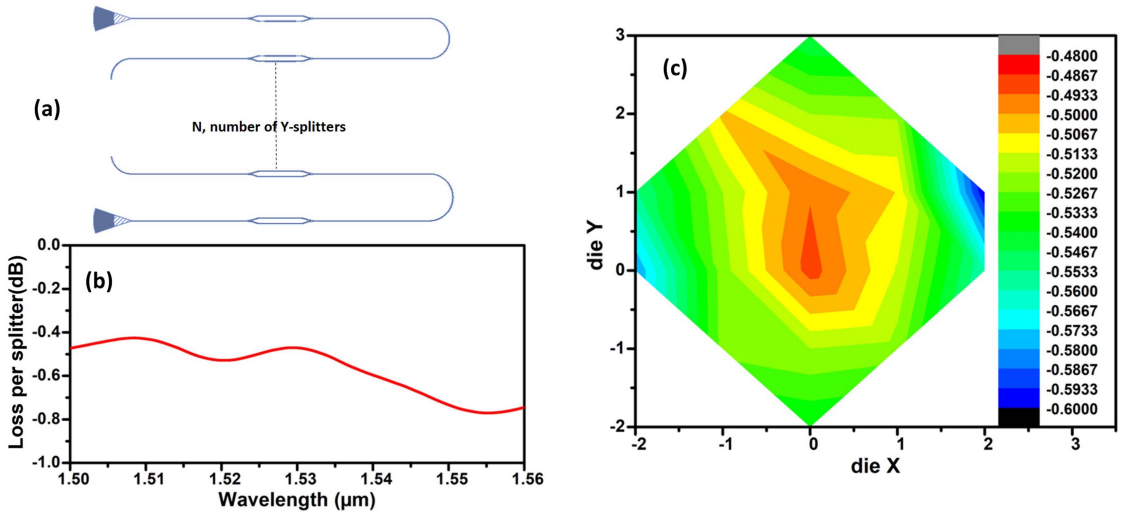

Fig. 6. (a) Schematic of the cascaded MZIs used to measure insertion losses, (b) measured loss per splitter over the wavelength range 1.50 μm - 1.56 μm, and (c) contour plot of the measured insertion loss in dB of the splitter across the wafer at a wavelength of 1550 nm.

splitting ratio close to 3 dB is achieved for the TE polarization over the measured bandwidth. Moreover, the power measured in each output arm was equal, and thus the results overlap in Fig. 5(a). The MZI transmission spectra for the TE polarization, excluding the coupling loss, is shown in Fig. 5(d). The length difference between the arms of the MZI (Δ L) is 120 μm. From the spectrum, an ER of 18 to 30 dB was obtained over a wavelength range of 60 nm. An average ER of 24 dB indicates that the power splitting ratio is close to 3 dB [3], [35], which matches the simulation results. The free spectral range of the MZI was 7.7 nm.

The sub -0.5 dB loss of a single device is challenging to measure; hence, we used cascaded splitters (see Fig. 6(a)) where N = 0, 8, 16 and 24 is the number of splitters in the test structure. The transmission spectrum of each set of cascaded splitters was measured experimentally and then the transmission as a function of the number of splitters was extracted for every measured wavelength. The insertion loss for one device is calculated by determining the slope of this data [37]. Fig. 6(b) shows the insertion loss per splitter as a function of wavelength. The insertion loss varies from 0.40 to 0.72 dB. The experimental loss of the device is approximately 0.12 dB more than the simulation results. This difference is most likely due to scattering caused by the sidewall roughness and changes in the geometry of the slot waveguides caused by fabrication variations. A contour plot of the insertion loss of devices as a function of their position on the wafer at a wavelength of 1550 nm is presented in Fig. 6(c). From the contour plot, we can see that the insertion loss varies

TABLE II
PERFORMANCE COMPARISON OF STATE-OF-THE-ART SPLITTERS

Parameters / References	Technology and core thickness (nm)	Structure/type	Polarization and average Insertion loss	Bandwidth (nm) Simulation and test	Footprint (WxL) $(\mu m)^2$	Minimum feature size	Possibility of fabrication through commercial silicon photonic processes
State of the art strip-slot waveguide splitters							
[34]	Silicon on Insulator thickness: 250nm	MMI junction with an embedded inverse-tapered Subwavelength Grating	Polarization insensitive 0.39 dB	200 nm; 1450-1650 nm	2.6 µm x 4.92 µm	±56 nm (not fabricated)	No
State of the art power splitter designs							
[38]	Silicon on Insulator thickness: 220nm	Y-junction	TE: 0.28 ± 0.02 dB.	80 nm bandwidth, ranging from 1500 nm to 1580 nm.	1.2 µm x 2 µm.	200 nm	yes
[40]	Silicon on Insulator thickness: 220 nm	Y-junction	TE: 0.19 TM:0.14	500 nm bandwidth ranging from 1200-1700 nm	5 µm x 2 µm	0.05 µm	No
[41]	Silicon on Insulator thickness: 220 nm	Directional coupler	TE: 0.35 TM:0.35	100 nm bandwidth ranging from 1500-1600 nm	29.4 µm x 0.6 µm	0.4 µm	Yes
[42]	Silicon on Insulator thickness: 220 nm	Adiabatic coupler	TE: 0.20	100 nm bandwidth ranging from 1500-1600 nm	25 µm x 2 µm	0.1 µm	No
[43]	Silicon on Insulator thickness: 220 nm	Adiabatic coupler	TE: 0.11	500 nm bandwidth ranging from 1200-1700 nm	35 µm x 7 µm	0.1 µm	No
[44]	Silicon on Insulator thickness: 340 nm	MMI coupler	TE: 0.14	NA	293 µm x 6 µm	0.7 µm	No
[45]	Silicon on Insulator thickness: 320 nm	MMI coupler	NA	NA	890 µm x 30 µm	NA	No
[46]	Silicon on Insulator thickness: 220 nm	MMI coupler	TE:0.16 TM:0.21	100 nm bandwidth ranging from 1500-1600 nm	6.6 µm x 2.6 µm	0.3 µm	Yes
[36]	Silicon on Insulator thickness: 220 nm	MMI based splitter	TE: 0.26 TM:0.16	400 nm bandwidth ranging from 1300-1700 nm	1.8 µm x 1.3 µm	0.2 µm	Yes
State of the art strip-slot mode converters							
[28]	Silicon on Insulator thickness: 250 nm	MMI based strip-slot converter	TE: 0.39dB TM: 0.35dB	125 nm bandwidth ranging from 1475-1600 nm	1.3 µm x 4 µm	100 nm	No
[30]	Silicon on Insulator thickness: 250 nm	Adiabatic taper bases mode converter	TE: 0.54 dB	500 nm bandwidth ranging from 1200-1700 nm	0.7 µm x 8 µm	20 nm	No
[31]	Silicon on Insulator thickness: 220 nm	Direct coupler	TE: 0.54 dB	200 nm bandwidth ranging from 1450-1650 nm	0.8 µm x 2 µm	50 nm	Yes
[26]	Silicon on Insulator thickness: 110 nm	Grated MMI based splitter+ grated strip-slot mode converter	4.6 dB/cm	100 nm bandwidth ranging from 1500-1600 nm	16 µm x 8 µm	120 nm	No
[24]	Silicon on Insulator thickness: 210 nm	MMI based splitter + adiabatic transition mode converter	NA	15 nm bandwidth ranging from 1540-1555 nm	Splitter: 6 µm x 24 µm Strip slot converter: 50 µm x 1.35 µm	70 nm	No
[47]	Silicon on Insulator and Polymer based Thickness 2 µm	Y-branch based splitter + adiabatic transition mode converter	0.9 dB	10 nm bandwidth ranging from 1330-1340 nm	Splitter: 2 µm x 2 µm Strip slot converter: 1 µm x 135 µm	20 nm	No
This work	**Silicon on Insulator**	**MMI junction**	**TE: 0.50±0.05**	**400 nm bandwidth ranging from 1300-1700nm**	**1.6 µm x 2 µm**	**150 nm (slot width)**	**Yes**

between 0.48 and 0.59 dB. The average insertion loss is 0.53 dB with a standard deviation of 0.03 dB. Those small fluctuations across the wafer confirm that this device is not very sensitive to fabrication variations.

IV. CONCLUSION

Many efficient silicon photonic power splitters have been reported in the literature, and Table II summarizes the performance and attributes of various state-of-the devices. The device presented here achieves comparable or even lower losses than several designs [36], [38], [46]. Furthermore, its broad bandwidth of 400 nm (ranging from 1300 nm to 1700 nm) exceeds or matches the capabilities of previously reported devices [28], [34], [40], [41]. Despite its remarkable performance, the proposed design maintains a compact footprint of 1.6 μm $\times$ 2 μm. Its small size along with the limited number of modes excited through the transition region and the wide wavelength range considered during the optimization helped maximize its operating bandwidth. Additionally, the potential for fabrication through a commercial silicon photonic process adds practicality, similar to designs in [36], [38], and [46]. This is a significant advantage over the silicon-based strip-to-slot power splitter proposed in [34], which used SWG. However, that design achieved polarization insensitivity over a bandwidth of 105 nm. While individual strip-slot converters and splitters have demonstrated impressive performance in their respective functions, their integration to create a strip-to-slot splitter introduces challenges related to increased losses and wavelength matching.

In summary, we demonstrated a low-loss, broadband, and compact 50–50 MMI splitter junction to interface a silicon strip waveguide with two slot waveguides. The device performance was measured experimentally over a range of 60 nm. It exhibits a low loss of 0.50 $\pm$ 0.03 dB at 1550 nm. This component

can be used to implement efficient MZI sensors or nonlinear optical devices. Since there are no adiabatic transition regions with narrow rails in this design, this relaxes the fabrication requirements, avoid the extra losses from having to use a separate strip-to-slot mode converter, and reduces the total size of the device significantly. Thus, this splitter design is promising for high density applications.

Acknowledgment

The authors would like to thank CMC Microsystems for providing access to the silicon photonic fabrication process.

References

[1] T. Li et al., "Low-voltage, high speed, compact silicon modulator for BPSK modulation," *Opt. Exp.*, vol. 21, no. 20, pp. 23410–23415, 2013, doi: 10.1364/OE.21.023410.

[2] S. Chen, Y. Shi, S. He, and D. Dai, "Compact monolithically-integrated hybrid (de) multiplexer based on silicon-on-insulator nanowires for PDM-WDM systems," *Opt. Exp.*, vol. 23, no. 10, pp. 12840–12849, 2015, doi: 10.1364/OE.23.012840.

[3] J. Wang et al., "Novel ultra-broadband polarization splitter-rotator based on mode-evolution tapers and a mode-sorting asymmetric Y-junction," *Opt. Exp.*, vol. 22, no. 11, pp. 13565–13571, 2014, doi: 10.1364/OE.22.013565.

[4] B. Chen, T. Tang, and H. Chen, "Flexible photonic crystal waveguide branches with arbitrary branching angles," *Opt. Lett.*, vol. 34, no. 13, pp. 1952–1954, 2009, doi: 10.1364/OL.34.001952.

[5] B. Chen, L. Huang, Y. Li, C. Liu, and G. Liu, "Flexible optical waveguide beam splitters based on directional coupling," *J. Opt. Soc. America B.*, vol. 28, no. 11, pp. 2680–2684, 2011, doi: 10.1364/JOSAB.28.002680.

[6] P.-G. Luan and K.-D. Chang, "Periodic dielectric waveguide beam splitter based on co-directional coupling," *Opt. Exp.*, vol. 15, no. 8, pp. 4536–4545, 2007, doi: 10.1364/OE.15.004536.

[7] L. Tao, A. R. Zakharian, M. Fallahi, J. V. Moloney, and M. Mansuripur, "Multimode interference-based photonic crystal waveguide power splitter," *J. Lightw. Technol.*, vol. 22, no. 12, pp. 2842–2846, Dec. 2004, doi: 10.1109/JLT.2004.834479.

[8] I. Park et al., "Photonic crystal power-splitter based on directional coupling," *Opt. Exp.*, vol. 12, no. 15, pp. 3599–3604, 2004, doi: 10.1364/OPEX.12.003599.

[9] T. B. Yu, Q. J. Wang, J. Zhang, J. Y. Yang, and S. F. Yu, "Ultracompact 2 × 2 photonic crystal waveguide power splitter based on self-imaging effect realized by asymmetric interference," *IEEE Photon. Technol. Lett.*, vol. 23, no. 16, pp. 1151–1153, Aug. 2011, doi: 10.1109/LPT.2011.2154360.

[10] S. Y. Lin, E. Chow, J. Bur, S. G. Johnson, and J. D. Joannopoulos, "Low-loss, wide-angle Y splitter at ~1.6-μm wavelengths built with a two-dimensional photonic crystal," *Opt. Lett.*, vol. 27, no. 16, pp. 1400–1402, 2002, doi: 10.1364/OL.27.001400.

[11] Z. Han and S. He, "Multimode interference effect in plasmonic subwavelength waveguides and an ultra-compact power splitter," *Opt. Commun.*, vol. 278, no. 1, pp. 199–203, 2007, doi: 10.1016/j.optcom.2007.05.058.

[12] S. I. Bozhevolnyi, V. S. Volkov, E. Devaux, J.-Y. Laluet, and T. W. Ebbesen, "Channel plasmon subwavelength waveguide components including interferometers and ring resonators," *Nature*, vol. 440, no. 7083, pp. 508–511, 2006, doi: 10.1038/nature04594.

[13] V. R. Almeida, Q. Xu, C. A. Barrios, and M. Lipson, "Guiding and confining light in void nanostructure," *Opt. Lett.*, vol. 29, no. 11, pp. 1209–1211, 2004, doi: 10.1364/OL.29.001209.

[14] Q. Xu, V. R. Almeida, R. R. Panepucci, and M. Lipson, "Experimental demonstration of guiding and confining light in nanometer-size low-refractive-index material," *Opt. Lett.*, vol. 29, no. 14, pp. 1626–1628, 2004, doi: 10.1364/OL.29.001626.

[15] T. Claes, J. G. Molera, K. D. Vos, E. Schacht, R. Baets, and P. Bienstman, "Label-free biosensing with a slot-waveguide-based ring resonator in silicon on insulator," *IEEE Photon. J.*, vol. 1, no. 3, pp. 197–204, Sep. 2009, doi: 10.1109/JPHOT.2009.2031596.

[16] H. Zengzhi and X. Jinsong, "Sub-50-nm wide slot waveguides with good optical isolation on silicon on insulator," *Proc. SPIE*, vol. 55, no. 8, 2016, Art. no. 087102, doi: 10.1117/1.OE.55.8.087102.

[17] D. Dai, Z. Wang, and J. E. Bowers, "Ultrashort broadband polarization beam splitter based on an asymmetrical directional coupler," *Opt. Lett.*, vol. 36, no. 13, pp. 2590–2592, 2011, doi: 10.1364/OL.36.002590.

[18] T. Huang, Y. Wu, Y. Xie, and Z. Cheng, "A slot-waveguide-based polarization beam splitter assisted by epsilon-near-zero material," *Photon. Nanostructures - Fundamentals Appl.*, vol. 33, pp. 42–47, 2019, doi: 10.1016/j.photonics.2018.12.001.

[19] J. Feng, R. Akimoto, and H. Zeng, "Asymmetric silicon slot-waveguide-assisted polarizing beam splitter," *IEEE Photon. Technol. Lett.*, vol. 28, no. 12, pp. 1294–1297, Jun. 2016, doi: 10.1109/LPT.2016.2541672.

[20] Y. Xu, J. Xiao, and X. Sun, "Compact polarization beam splitter for silicon-based slot waveguides using an asymmetrical multimode waveguide," *J. Lightw. Technol.*, vol. 32, no. 24, pp. 4282–4288, Dec. 2014, [Online]. Available: http://www.osapublishing.org/jlt/abstract.cfm?URI=jlt-32-24-4282

[21] Z. Ge, X. Li, S. Li, M. Liu, J. Si, and L. Zhang, "On-chip polarization beam splitter with multimode operation in a SOI waveguide," *Japanese J. Appl. Phys.*, vol. 58, no. 1, 2018, Art. no. 010905, doi: 10.7567/1347-4065/aaef92.

[22] S. Lin, J. Hu, and K. B. Crozier, "Ultracompact, broadband slot waveguide polarization splitter," *Appl. Phys. Lett.*, vol. 98, no. 15, 2011, Art. no. 151101, doi: 10.1063/1.3579243.

[23] Q. Liu et al., "Highly sensitive Mach–Zehnder interferometer biosensor based on silicon nitride slot waveguide," *Sensors Actuators B: Chem.*, vol. 188, pp. 681–688, 2013, doi: 10.1016/j.snb.2013.07.053.

[24] J.-M. Lee, "Ultrahigh temperature-sensitive silicon MZI with titania cladding," *Front. Mater.*, vol. 2, 2015, Art. no. 36, doi: 10.3389/fmats.2015.00036.

[25] N. Malviya and V. Priye, "Efficient design of silicon slot waveguide optical modulator," *Opto- Electron. Rev.*, vol. 25, no. 4, pp. 285–289, 2017, doi: 10.1016/j.opelre.2017.08.001.

[26] T. Baehr-Jones et al., "Nonlinear polymer-clad silicon slot waveguide modulator with a half wave voltage of 0.25V," *Appl. Phys. Lett.*, vol. 92, no. 16, 2008, Art. no. 163303, doi: 10.1063/1.2909656.

[27] C. Koos et al., "All-optical high-speed signal processing with silicon–organic hybrid slot waveguides," *Nature Photon.*, vol. 3, no. 4, pp. 216–219, 2009, doi: 10.1038/nphoton.2009.25.

[28] Q. Deng, L. Liu, X. Li, and Z. Zhou, "Strip-slot waveguide mode converter based on symmetric multimode interference," *Opt. Lett.*, vol. 39, no. 19, pp. 5665–5668, 2014, doi: 10.1364/OL.39.005665.

[29] Y. Liu and J. Yu, "Low-loss coupler between fiber and waveguide based on silicon-on-insulator slot waveguides," *Appl. Opt.*, vol. 46, no. 32, pp. 7858–7861, 2007, doi: 10.1364/AO.46.007858.

[30] Z. Wang, N. Zhu, Y. Tang, L. Wosinski, D. Dai, and S. He, "Ultracompact low-loss coupler between strip and slot waveguides," *Opt. Lett.*, vol. 34, no. 10, pp. 1498–1500, 2009, doi: 10.1364/OL.34.001498.

[31] K. Han et al., "A strip-slot direct mode coupler," in *Proc. 2016 Conf. Lasers Electro- Opt.*, Jun. 2016 pp. 1–2.

[32] Q. Deng, Q. Yan, L. Liu, X. Li, J. Michel, and Z. Zhou, "Robust polarization-insensitive strip-slot waveguide mode converter based on symmetric multimode interference," *Opt. Exp.*, vol. 24, no. 7, pp. 7347–7355, 2016, doi: 10.1364/OE.24.007347.

[33] V. Mere, R. Kallega, and S. K. Selvaraja, "A novel scheme to excite SOI slot waveguide mode," in *Proc. IEEE 14th Int. Conf. Group IV Photon.*, Aug. 2017, pp. 137–138, doi: 10.1109/GROUP4.2017.8082234.

[34] Y. Xu and J. Xiao, "An ultracompact polarization-insensitive silicon-based strip-to-slot power splitter," *IEEE Photon. Technol. Lett.*, vol. 28, no. 4, pp. 536–539, Feb. 2016, doi: 10.1109/LPT.2015.2502983.

[35] L. B. Soldano and E. C. M. Pennings, "Optical multi-mode interference devices based on self-imaging: Principles and applications," *J. Lightw. Technol.*, vol. 13, no. 4, pp. 615–627, Apr. 1995, doi: 10.1109/50.372474.

[36] D. P. Nair and M. Ménard, "A compact low-loss broadband polarization independent silicon 50/50 splitter," *IEEE Photon. J.*, vol. 13, no. 4, 2021, Art. no. 6600207, doi: 10.1109/JPHOT.2021.3091539.

[37] Z. Xiao et al., "Ultra-compact low loss polarization insensitive silicon waveguide splitter," *Opt. Exp.*, vol. 21, no. 14, pp. 16331–16336, 2013, doi: 10.1364/OE.21.016331.

[38] Y. Zhang et al., "A compact and low loss Y-junction for submicron silicon waveguide," *Opt. Exp.*, vol. 21, no. 1, pp. 1310–1316, 2013, doi: 10.1364/OE.21.001310.

[39] J. Avad, M. Demirtaş, N. Kosku Perkgöz, and F. Ay, "A realistic approach for designing a single-mode Y-branch for weakly guiding material system using particle swarm algorithm," *Opt. Quantum Electron.*, vol. 52, no. 2, 2020, Art. no. 74, doi: 10.1007/s11082-019-2181-5.

[40] Y. Wang, S. Gao, K. Wang, and E. Skafidas, "Ultra-broadband and low-loss 3 dB optical power splitter based on adiabatic tapered silicon waveguides," *Opt. Lett.*, vol. 41, no. 9, pp. 2053–2056, 2016, doi: 10.1364/OL.41.002053.

[41] Y. Kim, M. H. Lee, Y. Kim, and K. H. Kim, "High-extinction-ratio directional-coupler-type polarization beam splitter with a bridged silicon wire waveguide," *Opt. Lett.*, vol. 43, no. 14, pp. 3241–3244, 2018, doi: 10.1364/OL.43.003241.

[42] L. Xu et al., "Compact high-performance adiabatic 3-dB coupler enabled by subwavelength grating slot in the silicon-on-insulator platform," *Opt. Exp.*, vol. 26, no. 23, pp. 29873–29885, 2018, doi: 10.1364/OE.26.029873.

[43] H. Yun, L. Chrostowski, and N. A. F. Jaeger, "Ultra-broadband 2 × 2 adiabatic 3dB coupler using subwavelength-grating-assisted silicon-on-insulator strip waveguides," *Opt. Lett.*, vol. 43, no. 8, pp. 1935–1938, 2018, doi: 10.1364/OL.43.001935.

[44] M. S. Rouifed et al., "Ultra-compact MMI-based beam splitter demultiplexer for the NIR/MIR wavelengths of 1.55 μm and 2 μm," *Opt. Exp.*, vol. 25, no. 10, pp. 10893–10900, 2017, doi: 10.1364/OE.25.010893.

[45] N. Najeeb, Y. Zhang, C. J. Mellor, and T. M. Benson, "Design, fabrication and demonstration of a 1x20 multimode interference splitter for parallel biosensing applications," *J. Phys.: Conf. Ser.*, vol. 679, no. 1, 2016, Art. no. 012027. [Online]. Available: http://stacks.iop.org/1742-6596/679/i=1/a=012027

[46] S. Hassan and D. Chack, "Design and analysis of polarization independent MMI based power splitter for PICs," *Microelectronics J.*, vol. 104, 2020, Art. no. 104887, doi: 10.1016/j.mejo.2020.104887.

[47] J. Han et al., "Highly sensitive liquid M-Z waveguide sensor based on polymer suspended slot waveguide structure," *Polymers*, vol. 14, 2022, Art. no. 3967.